



Preparation of stable and highly active Ni/CeO₂ catalysts by glow discharge plasma technique for glycerol steam reforming

Bo Wang^{a,1}, Yingying Xiong^{a,1}, Yaoyao Han^a, Jingping Hong^{a,*}, Yuhua Zhang^a, Jinlin Li^a, Fangli Jing^{b,*}, Wei Chu^b

^a Key Laboratory of Resources Green Conversion and Utilization of the State Ethnic Affairs Commission & Ministry of Education, South-Central University for Nationalities, Wuhan, Hubei, 430073, China

^b School of Chemical Engineering, Sichuan University, No. 24 South Section 1, Yihuan Road, Chengdu, Sichuan, 610065, China

ARTICLE INFO

Keywords:

Glycerol steam reforming
Nickel-based catalyst
Glow discharge plasma
Nickel source
Ceria

ABSTRACT

CeO₂ nanorods supported nickel catalysts were prepared by wetness impregnation method, using nickel nitrate and nickel chloride as nickel sources. The dried catalyst precursors were decomposed either by thermal calcination or glow discharge plasma technique. The effects of precursor decomposition methods and nickel sources on the catalytic performance of glycerol steam reforming were then investigated. Characterization and catalytic results showed that glow discharge plasma treatment instead of thermal calcination enhanced the nickel dispersion, improved the Ni-Ce interaction and led to the formation of Ni-O-Ce composite, which could both enhance the H₂ selectivity and restrain the coke deposition during reaction. Thus, no deactivation was observed on the two plasma treated catalysts throughout the tests. Nickel source may influence both rate of particle sintering and carbonaceous deposition during reaction; fast nickel sintering but slower coke deposition was found on the catalysts prepared from nickel chloride, and coke deposition was more detrimental to active sites decrease than nickel sintering.

1. Introduction

Hydrogen is a clean and green fuel, and due to its environmental advantages and high efficiency, H₂ can be used as a potential energy carrier and its demand is continued to increase [1–3]. Hydrogen can be produced via various routes, taking environmental and economic concerns into consideration, conversion of biomass-derived feedstock gained particular research interests in recent years [4–8]. Glycerol is the major byproduct during biodiesel production, and with increasing biodiesel productivity, the productivity of glycerol is also increased and leads to a significant oversupply, as a result, the price of crude glycerol is ongoing declined. To obtain both economic and environmental benefits, glycerol can be used as a viable biomass-derived feedstock to produce hydrogen via steam reforming [8,9]. The overall reaction of glycerol steam reforming (GSR) is an endothermic reaction, and can be expressed as that 1 mol of glycerol reacts with 3 mol of water and reversibly forms 7 mol of hydrogen and 3 mol of carbon dioxide. This reaction is further composed by an endothermic glycerol decomposition reaction and an exothermic water gas shift reaction [9–11].

Concerning the catalysts for glycerol steam reforming, great

endeavors have been carried out for the development of cheap, highly active, selective and deactivation-resistant catalysts, and it remains a challenge so far. Many researchers were focused on Ni-based catalysts, since they are cost effective; besides, they have excellent activity in the cleavage of the bonds of C–C, C–H and H–O. [10–14] However, sintering and coke deposition are inevitable occurred on nickel catalysts, exploration of an effective way to minimize these problems is still a challenge and has attracted much concern in recent years.

Catalyst preparation process has significant influences on the catalyst structure and properties, which would directly affect the catalytic performance, including activity, selectivity and stability. Supported catalysts, including Ni-based catalysts for GSR are most commonly prepared by impregnation method [15,16]. During the preparation, a solution of Ni salt is added to a solid support, followed by drying and calcination to remove solvents and decompose nickel salt. This technique is simple and easy to reproduce, however, it usually accompanies with the drawback of less active sites and easy to deactivate owing to the weak metal – support interaction and possible loss of active surface metals. Other catalyst preparation techniques can achieve the efficient dispersion of metals on the supports and good catalyst stability, but

* Corresponding authors.

E-mail addresses: jingpinghong@mail.scuec.edu.cn (J. Hong), fangli.jing@scu.edu.cn (F. Jing).

¹ These authors are contributed equally to this work.

these techniques are mostly quite complex, with high chemicals and time consumption [5,17–19]. Thus, development of an optimized technique for the synthesis of high dispersed catalyst with high GSR activity and stability is with high potential.

Glow discharge plasma, as a kind of low-temperature plasma, is an environmental friendly technique with low energy consumption and shortened preparation time for surface modification or production of variable nanostructures [20–22]. Glow discharge is generated by the passage of electric current through a gas, applying a voltage ($>$ striking voltage) between two electrodes at low pressure. In plasma field, the excited and ionized particles including free electrons, ions, radicals and neutral species carry enough energy to give rise to chemical reactions on the solid surface and change the properties of materials. Therefore, the use of plasma technology in catalyst preparation has previously attracted much attention [23–25].

Herein, our present work is focused on selection of appropriate nickel precursors and exploration of glow discharge plasma technique for better glycerol steam reforming performance. We have synthesized two Ni/CeO₂ catalysts, using either nickel nitrate or nickel chloride as nickel source, and the nickel salts were decomposed by either thermal calcination or glow discharge plasma technique. Their catalytic behavior including glycerol activity, H₂ selectivity and particularly the stability was thoroughly studied by various characterization techniques.

2. Experimental section

2.1. CeO₂ preparation

400 mL of 6 mol/L NaOH solution and 200 mL of 0.3 mol/L Ce (NO₃)₃·H₂O solution were mixed and magnetic stirred for 30 min, then the mixture was transferred into an autoclave and crystallized at 120 °C for 24 h. The precipitate was washed thoroughly using deionized water, followed by drying in an oven at 60 °C for 24 h and calcining in a muffle furnace at 600 °C for 4 h, the obtained nanorods structured CeO₂ was denoted as CeO₂.

2.2. Catalyst preparation

CeO₂ supported Ni-based catalyst precursors were prepared using nickel nitrate hexahydrate or nickel chloride hexahydrate as nickel sources via incipient wetness impregnation method. The dried precursors were respectively divided into two parts, one part was calcined in a muffle furnace at 550 °C for 4 h, the obtained samples were labeled as Ni-N/CeO₂-C and Ni-Cl/CeO₂-C, in which N corresponded to the nickel source of nickel nitrate, Cl assigned to the nickel source of nickel chloride, and C indicated the process of calcinations. The other part of the precursors was treated by glow discharge plasma for 2 h, the treating parameters are listed in Table 1, and the as-prepared catalysts were marked as Ni-N/CeO₂-P and Ni-Cl/CeO₂-P, in which P corresponded to the process of plasma treatment. In these four catalysts, the nominal nickel loading was 10 wt. %.

2.3. Characterization

Structure and properties of the supports and catalysts were characterized by scanning electron microscopy (SEM), N₂ physisorption, X-ray diffraction (XRD), transmission electron microscopy (TEM), X-ray photoelectron spectroscopy (XPS), hydrogen temperature-programmed

reduction (H₂-TPR), Raman spectroscopy, hydrogen temperature programmed desorption (H₂-TPD) and oxygen titration [26,27].

SEM photographs of the catalysts were performed on a HITACHI-48005 apparatus. Energy dispersive spectroscopy (EDS) images were obtained on Zeiss Supra 55 spectrometer. N₂ adsorption-desorption isotherms were obtained from a Quanta chrome Autosorb-1-C-TCD-MS instrument. XRD patterns at the 2 θ range from 20° to 80° with a step size of 0.02° were recorded on a Bruker Advanced D8 diffractor meter equipped with a Cu K α radiation source (λ = 0.154056 nm). TEM images of pre-reduced catalysts were carried out on a FEI Tecnai G2-20 microscope (200 kV). XPS spectra was recorded on a VG Mutilab 2000 spectrometer with monochromatic Al K α (1486.6 eV) radiation source.

H₂-TPR profiles in the temperature range of 50–1000 °C were documented on a Zeton Altamira AMI-200 apparatus, with a gaseous mixture of 5% H₂ in N₂ using as reductant. H₂-TPD followed by oxygen titration were performed also on the Zeton Altamira AMI-200 unit. The catalysts were firstly reduced at 450 °C for 5 h and cooled down to 50 °C in a hydrogen flow. H₂-TPD was recorded from 50 to 450 °C. Subsequently, the reduced catalysts were purged with oxygen at 450 °C until there was no further consumption of O₂, the amount of oxygen consumed was then determined, and the data was used to calculate Ni reduction percentage by assuming that the Ni⁰ reoxidized to NiO. Uncorrected Ni dispersion of reduced Ni/CeO₂ catalysts was calculated based on the hydrogen uptake using the method reported in refs. [1,28,29], and Ni particle size was calculated by the formula of $d(\text{Ni}) (\text{nm}) = 101/D_{\text{Ni}}(\%)$ [30], assuming Ni in spherical particles.

Raman spectra of the spent catalysts were obtained on a Netzsch 209F3 instrument using a 530 nm semiconducting laser, and their TGA and DTG curves were gotten from a TA apparatus of Thermo Fisher Scientific DXR2XI.

2.4. Catalytic tests

The catalytic performance of the four catalysts on steam reforming of glycerol was conducted in a fixed-bed stainless steel reactor (i.d.: 10 mm) under ambient pressure [11]. Typically, 200 mg of the specified catalyst was diluted with 1.8 g of silica sand (ϕ = 0.30 mm) and loaded into the temperature constant section of reactor. Before reaction, the catalyst was in-situ reduced at 450 °C in H₂ flow. When the reduction finished, the catalyst bed was maintained at the same temperature (450 °C), and then the feed reactant (10 wt. % glycerol in water) was pumped into a vaporization chamber (250 °C) with a flow rate of 3.0 mL/h (WHSV = 15 h⁻¹), to ensure that there was no external diffusion limitations. A N₂ flow with a flow rate of 60 mL/min was used to drive the vaporized mixture into the reactor. The gaseous products (mainly H₂, CH₄, CO and CO₂) were analyzed by an online GC equipped with thermal conductivity detector (TCD) through two packed columns (Porapak N: 4 mm o.d., 2 m length, Molecular sieves 13X: 4 mm o.d., 2 m length). The un-reacted glycerol and liquid-phase products were condensed in a cold trap (0 °C) and further analyzed using an offline GC with flame ionization detector (FID) equipped with a capillary column (KB InnoWAX: 0.35 mm i.d., 30 m length). The reaction data in table were collected at 8 h time on stream to ensure that the catalysts were experienced the preliminary deactivation.

Table 1

Glow discharge plasma treating parameters on Ni/CeO₂ catalyst precursors.

Input peak voltage (V)	Input peak power (W)	Duty factor (%)	Pressure (Pa)	Treating duration (h)	Treating temperature (°C)	Treating atmosphere	Total energy consumption (KW)
150	500	25	150	2	400	Air	1.125

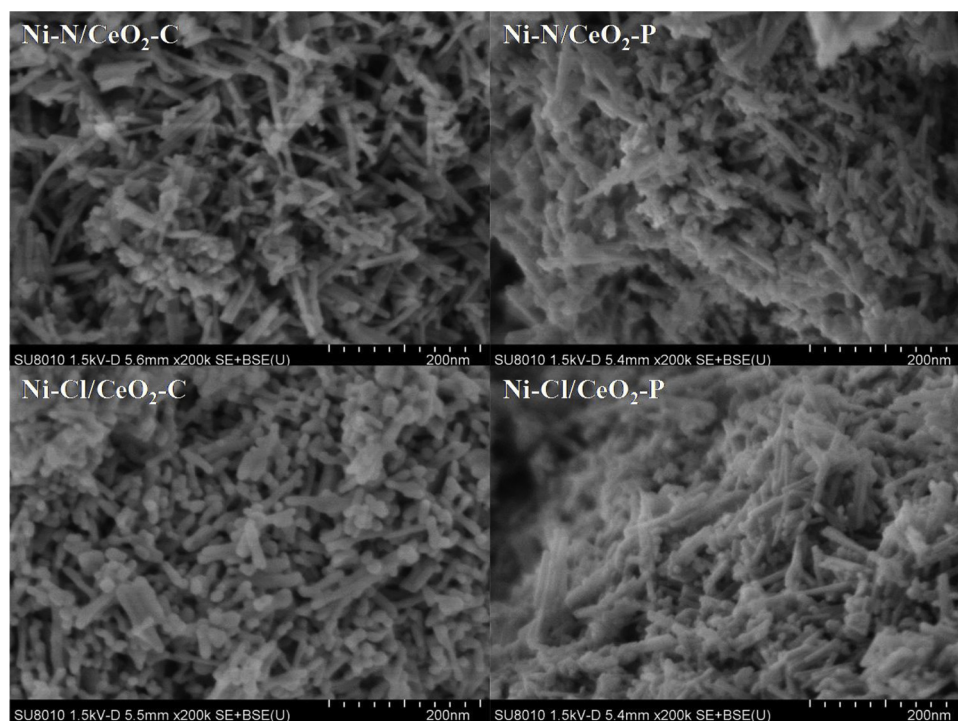


Fig. 1. SEM photographs of the Ni/CeO₂ catalysts.

3. Result and discussion

3.1. Structure and properties of fresh catalysts

Morphology of the nickel particles and CeO₂ supports were examined firstly by SEM, the images of the four catalysts are shown in Fig. 1. After Ni loading and thermal calcination or glow discharge plasma treatment, the CeO₂ supports are maintained the shape of nanorods. Ni particles were seemed to be adhered on the nanorods, and they were found to be extremely larger and aggregated on the Ni-Cl/CeO₂-C catalyst. EDS of the elements (Fig. S1) confirmed the above observation, aggregation of nickel species was only observed on the calcined sample prepared with nickel chloride (Ni-Cl/CeO₂-C), while homogeneous dispersion of Ni species was revealed both on plasma treated catalysts and the calcined one using nickel nitrate as source.

Porous structure of the support and catalysts were characterized by N₂ physisorption. As shown in Fig. S2, both CeO₂ material and the supported Ni/CeO₂ catalysts show irregular pore size distributions and representative type V isotherms with H3 hysteresis loops according to the classification of IUPAC, indicating the presence of irregular mesopores generated by the stacking of CeO₂ nanorods. After Ni loading, BET surface area, particularly pore volume and average pore diameter were remarkable decreased (Table 2), indicating the entering and blocking of the pores by nickel particles.

XRD patterns of CeO₂ support and the four Ni/CeO₂ catalysts were shown in Fig. 2. The diffraction peaks located at $2\theta = 28.5^\circ$, 33.1° , 47.5° , 56.3° , 59.1° , 69.4° , 76.7° , 79.1° and 88.4° , which corresponded to

the (111), (200), (220), (331), (222), (400), (331), (420) and (422) crystal facets of CeO₂, were clearly observed on both support and catalysts. Due to the significant lower intensity of nickel diffraction peaks, 2θ range of $35\text{--}45^\circ$ was enlarged (Fig. 2(b)), the peaks at $2\theta = 37.2^\circ$ and 43.3° attributing to (020) and (202) crystal facets of NiO could only be observed on the two calcined catalysts (Ni-N/CeO₂-C and Ni-Cl/CeO₂-C), and the NiO diffraction peaks on Ni-N/CeO₂-C were much broader, indicating higher nickel dispersion on Ni-N/CeO₂-C than that on the one using nickel chloride as source (Ni-Cl/CeO₂-C). Calculation of NiO particle size was based on Scherrer equation using the half-height peak width at $2\theta = 43.3^\circ$, and the data for Ni-N/CeO₂-C and Ni-Cl/CeO₂-C were 16.4 nm and 29.8 nm, respectively. No diffraction peaks assigned to nickel species were detected on the two plasma treated catalysts (Ni-N/CeO₂-P and Ni-Cl/CeO₂-P), indicating either high dispersion or weak crystallinity of Ni species after glow discharge plasma treatment.

To further obtain the information about nickel dispersion, TEM of the catalysts was performed and the images are shown in Fig. 3. Compared with the calcined samples (Fig. 3(a) (c)) and their plasma treated counterparts (Fig. 3(b) (d)), it is clearly demonstrated that plasma treatment led to the formation of homogeneously dispersed smaller nickel particles. Particle size distribution of nickel species (Fig. 3) showed that plasma treatment instead of thermal calcination led to a 42.6% decrease of NiO particle size on the ones using nickel nitrate as source, and a 40.6% decrease on the ones applying nickel chloride as precursor. Contrast of the catalysts with different nickel sources showed that the samples prepared from nickel chloride (Ni-Cl/CeO₂-C and Ni-Cl/CeO₂-P) owned larger NiO particle size than their counterparts from nickel nitrate (Ni-N/CeO₂-C and Ni-N/CeO₂-P). Although discrepancies were found on the specific values, the tendency from TEM findings was in good agreement with XRD results.

To further obtain the information about surface chemical environment and valence states, X-ray photoelectron spectroscopy (XPS) of the four fresh prepared Ni/CeO₂ catalysts was performed. C 1 s peak was set to 284.8 eV to calibrate the other elements, and the quantitative analyzed data obtained from peak-differentiating and imitating are listed in Table 3. Ni 2p_{3/2} XPS spectra (Fig. 4(a)) were deconvoluted to three

Table 2

Textural parameters of support and catalysts.

Material	S _{BET} (m ² /g)	Pore volume (cm ³ /g)	BJH pore size (nm)
CeO ₂	91.1	1.13	30.8
Ni-N/CeO ₂ -C	73.5	0.38	16.5
Ni-N/CeO ₂ -P	73.8	0.37	12.3
Ni-Cl/CeO ₂ -C	49.2	0.53	17.2
Ni-Cl/CeO ₂ -P	57.8	0.41	17.5

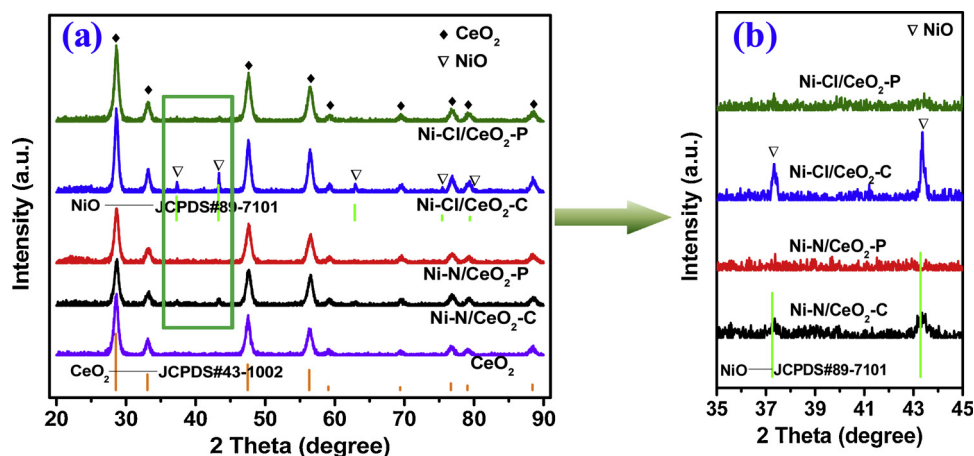


Fig. 2. XRD patterns of CeO₂ support and Ni/CeO₂ catalysts.

peaks, since metallic nickel, NiO and Ni(OH)₂ all had main peak centered at 855.5 eV, the attribution of Ni species was required to combined with basic understanding of the catalyst preparation. Besides the plasma treated catalysts, the calcined samples were thermal treated in air at 550 °C for 4 h, considering Ni(OH)₂ would be decomposed into NiO and H₂O at 230 °C, therefore, the peaks at 853.2–855.5 eV were attributed to multiplet-split Ni 2p_{3/2} peak of NiO, and the peak around 860.5 eV was its satellite peak [31,32]. Either plasma treatment or using nickel chloride as nickel source led a shift of Ni 2p_{3/2} binding energy of NiO to higher energies, indicating both methods could give rise to a stronger interaction between CeO₂ support and Ni species. The shift of Ni-Cl/CeO₂-P catalyst, which was prepared by nickel chloride and treated with plasma, was the most significant among the four catalysts studied in this work.

Ce 3d and O 1s XPS spectra of the four Ni/CeO₂ catalysts were also analyzed and are shown in Fig. S3. The Ce 3d XPS spectra (Fig. S3(a)) were fitted with eight peaks. The v peaks in the range of 878–899 eV were attributed to Ce 3d_{5/2} peaks and the u peaks between 899–920 eV were Ce 3d_{3/2} peaks. The peaks of v₁ and u₁ were assigned to Ce³⁺ species, while the other six peaks were ascribed to Ce⁴⁺ fractions [33]. Ce³⁺ and Ce⁴⁺ were co-existed on the surface of the four catalysts. The ratios of Ce³⁺/(Ce³⁺ + Ce⁴⁺) in Table 3 were calculated based on the formula reported in ref. [34], it was illustrated that the majority of Ce species were still in the state of Ce⁴⁺, and surface Ce³⁺ content was

Table 3

Surface analysis data of the four Ni/CeO₂ catalysts by XPS.

Catalyst	Ce ³⁺ /(Ce ³⁺ + Ce ⁴⁺)	O _{ads} /(O _{latt} + O _{ads})	Surface Ni _{oxidized} (%)	Surface Ni _{reduced} (%)
Ni-N/CeO ₂ -C	0.13	0.35	4.84	3.40
Ni-N/CeO ₂ -P	0.14	0.37	6.01	5.39
Ni-Cl/CeO ₂ -C	0.16	0.38	2.67	2.31
Ni-Cl/CeO ₂ -P	0.17	0.39	2.80	7.02

higher on plasma treated or nickel chloride prepared samples. Compared with Ni-N/CeO₂-C catalyst, the Ce 3d binding energy of the plasma treated catalysts and the catalysts prepared from nickel chloride was slightly shifted to higher values, which might be caused by the stronger Ni-CeO₂ interaction or incorporation of Ni²⁺ ions into CeO₂ [35].

As shown in Fig. S3(b), O 1s XPS peaks were analyzed and fitted into two peaks. The main peaks located around 529.0 eV were attributed to the lattice O bonded with metal cation, while the ones at around 530.0 eV were assigned to the adsorbed oxygen species. As shown in Table 3, the content of adsorbed oxygen was in the order of Ni-Cl/CeO₂-P > Ni-Cl/CeO₂-C > Ni-N/CeO₂-P > Ni-N/CeO₂-C, same tendency as surface Ce³⁺ content in these catalysts. It was reported that ceria is a

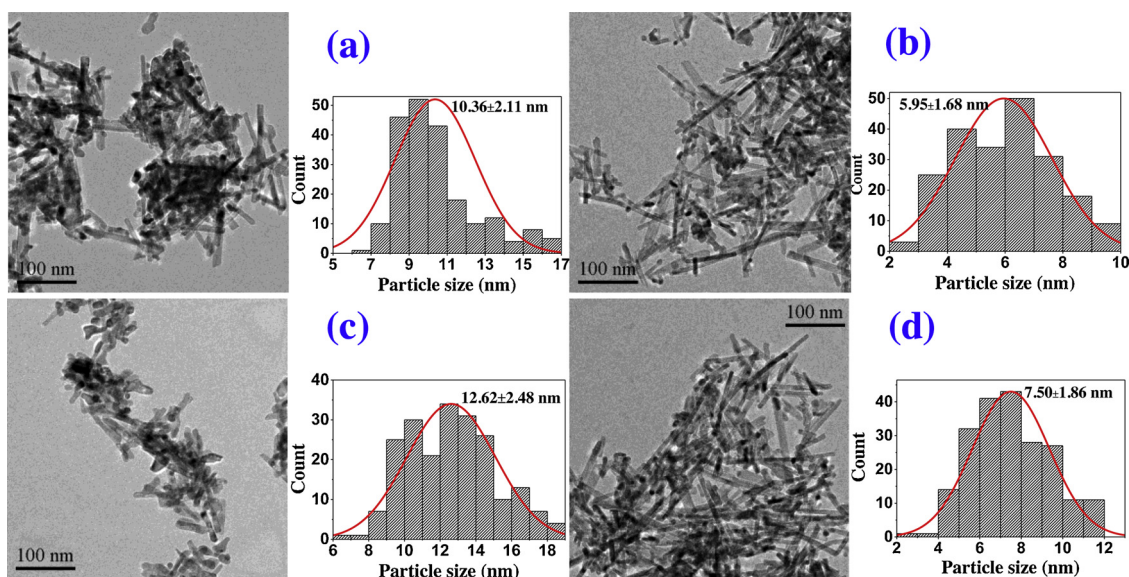


Fig. 3. TEM images and nickel particle size distributions of (a) Ni-N/CeO₂-C; (b) Ni-N/CeO₂-P; (c) Ni-Cl/CeO₂-C; (d) Ni-Cl/CeO₂-P.

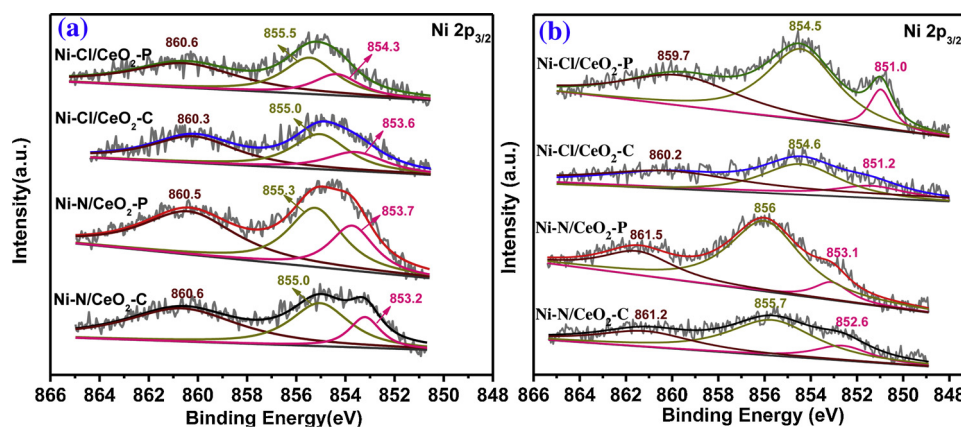


Fig. 4. Ni $2p_{3/2}$ XPS spectra of (a) oxidized and (b) reduced Ni/CeO₂ catalysts.

fluorite-type oxide with unique reversible $\text{Ce}^{3+}/\text{Ce}^{4+}$ redox pair, in which oxygen vacancies can be created under certain conditions [36], the concentration of oxygen vacancies was associated with the amount of surface Ce^{3+} [33,37]. Glow discharge plasma treatment as well as the nickel source could both influence the surface oxygen vacancies fraction, higher content of Ce^{3+} and adsorbed oxygen in plasma treated catalysts or Ni-Cl/CeO₂-C resulted in anchoring the Ni particles on the CeO₂ and lead to a strong interaction between metal and support [37].

It is known that active sites for GSR were located on metallic nickel, to better understand the properties of catalysts during reaction, XRD and Ni $2p_{3/2}$ XPS of reduced catalysts were performed. Before the measurements, the catalysts were pre-reduced in H₂ flow at 450 °C for 5 h, after cooled down to room temperature, the catalysts were passivated in 1% O₂/Ar flow. Except the diffraction peaks of CeO₂, only characteristic peaks attributed to Ni⁰ was observed on Ni-N/CeO₂-C, Ni-Cl/CeO₂-C and Ni-Cl/CeO₂-P catalysts (Fig. S4), their particle sizes calculated by Scherrer equation were listed in Table 6. As to Ni-N/CeO₂-P catalyst, no diffraction peak of Ni species was observed. XRD results of reduced catalysts showed that NiO was reduced into Ni⁰ under the same reduction conditions as reaction, and the nickel dispersion was in good accordance with the fresh prepared samples, no apparent sintering was detected. Ni $2p_{3/2}$ XPS spectra (Fig. 4(b)) show quite different surface properties of the catalysts prepared from different nickel precursors. It is documented that besides the main peak, the minor one at around 852 eV was assigned to metallic nickel [31], however, this peak on Ni-Cl/CeO₂ catalysts was shifted to ~ 1 eV lower and that on Ni-N/CeO₂ catalysts was shifted to ~ 1 eV higher. Since the reduced catalysts were passivated before XPS measurement, it is hard to precisely distinguish the surface nickel species. The surface Ni contents of reduced catalysts are listed in Table 3. The two plasma treated catalysts showed much more surface Ni than the calcined samples, consistent with XRD and TEM results. The discrepancy of this value on fresh plasma treated and reduced Ni-Cl/CeO₂-P catalyst may due to the non-uniform dispersion of nickel species on the support material.

H₂-TPR was used to investigate the reducibility of catalysts, the profiles are shown in Fig. 5. The reduction behavior of Ni/CeO₂ samples can be divided into four hydrogen consumption peaks (α_1 , α_2 , β , γ) [38]. The TPR spectrum (Fig. S5) of CeO₂ support confirmed that the weak γ peaks at above 700 °C were derived from the reduction of bulk CeO₂. β peaks were assigned to the reduction of bulk NiO, and α_1 , α_2 peaks were ascribed as the reduction of adsorbed oxygen in Ni-O-Ce composite [38,39]. Compared with thermal calcined samples, the α_1 and α_2 peaks were apparently stronger in two plasma treated catalysts, suggesting that Ni²⁺ species might be incorporated into the lattice of CeO₂ material and lead to the formation of Ni-O-Ce composite during plasma treatment, which resulted in the lattice distortion and an augment in both content of Ce^{3+} and adsorbed oxygen species, in good agreement with XPS findings. The arisen α_1 and α_2 peaks may imply

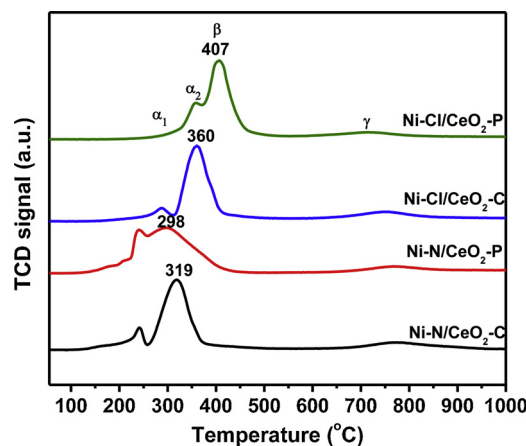


Fig. 5. TPR profiles of the four Ni/CeO₂ catalysts.

more Ni²⁺ incorporating into CeO₂ and stronger interaction between Ni and CeO₂ support in plasma treated catalysts. It is generally considered that stronger interaction between metal and support causes more difficult reduction of metal oxide, and the reduction temperatures usually shifts to higher values. The calcined catalysts followed this rule, Ni-Cl/CeO₂-C with stronger Ni-CeO₂ interaction showed H₂ consumption peaks at higher temperature (360 °C) than Ni-N/CeO₂-C (319 °C). However, as to the plasma treated catalysts, although the interaction between Ni and CeO₂ were enhanced, since they had more adsorbed surface oxygen species arising by the formation of Ni-O-Ce composite which could be easily reduced by H₂ at much lower temperature [38,39], the reducibility of NiO could also be improved. Therefore, the reduction temperature of Ni-N/CeO₂-P was decreased from 319 °C of calcined counterpart to 297 °C. As to Ni-N/CeO₂-P catalyst, even with abundant easily reducible adsorbed surface oxygen species, the too strong Ni-CeO₂ interaction originated both by plasma treatment and nickel chloride as precursor, drove the NiO reduction temperature of this sample to higher values (407 °C).

It is known that both the dispersion and reducibility of nickel species determine the final number of active sites for glycerol steam reforming reaction. To further understand the information about nickel dispersion and reducibility of the catalysts in GSR tests, H₂-TPD followed by O₂ titration were performed, the data are listed in Table 4. The H₂-TPD was conducted after reduction at 450 °C for 5 h, the same reduction conditions as in-situ reduction before GSR reaction. Since the uncorrected data are based on the assumption of complete reduction, the corrected Ni dispersion and particle size listed in Table 4 take the percentage of reduced nickel into consideration [40]. Nickel particle sizes in this work were estimated also by XRD, TEM. The data from XRD were calculated using Scherrer equation from the half-height width of

Table 4
H₂-TPD and O₂ titration results for four catalysts.

Catalyst	H ₂ desorbed (μmol/g)	D _{uncorrected} (%)	d _{uncorrected} (nm)	O ₂ uptake (μmol/g)	Reducibility (%)	D _{corrected} (%)	d _{corrected} (nm)
Ni-N/CeO ₂ -C	297.1	17.4	5.8	968.1	86.0	20.2	5.0
Ni-N/CeO ₂ -P	525.1	30.8	3.3	1052.2	93.5	33.0	3.1
Ni-Cl/CeO ₂ -C	179.2	10.5	9.6	887.9	74.2	14.1	7.1
Ni-Cl/CeO ₂ -P	398.0	23.4	4.3	1014.5	89.1	26.3	3.8

the most intense nickel diffraction peak (NiO or Ni²⁺). These values are volume mean diameter and small nickel particles (< 3 nm) would be missed because of significant XRD line broadening. Therefore, this method overestimated nickel particle size [41,42]. In addition, no detection of nickel diffraction peaks on fresh plasma treated catalysts may due to less crystallization of nickel particles by glow discharge plasma treatment [43]. Nickel particle size from TEM is number mean and it provides direct evidence for nickel dispersion. Whereas nickel particle size from H₂-TPD and O₂ titration is surface mean diameter, it is obtained by assuming the nickel particles in spherical morphology [29,44] and considering the H:Ni stoichiometry ratio of 1:1. As a consequence, this method may underestimate the nickel crystallite size [45]. In this work, although the nickel particle sizes obtained from three methods had some discrepancies in the absolute values, they showed the same variation tendency. In good agreement with the above XRD and TEM results, nickel dispersion was greatly enhanced by plasma treatment, and the catalysts prepared from nickel chloride had larger nickel particle size. Although stronger Ni - CeO₂ interaction and higher nickel dispersion were found on plasma treated catalysts, after reduction at 450 °C for 5 h, nickel reducibility was higher on these catalysts. The reduction degree of the plasma treated samples was increased from 86.0% of Ni-N/CeO₂-C to 93.5% of Ni-N/CeO₂-P, and 74.2% of Ni-Cl/CeO₂-C to 89.1% of Ni-Cl/CeO₂-P, respectively. The catalysts prepared from nickel nitrate had slightly higher reduction degree than the counterparts using nickel chloride as precursor. It should be noted that apart from metallic nickel, the oxygen vacancy of ceria will also consume oxygen, thus nickel reducibility on plasma treated catalysts with more oxygen vacancy may be overestimated. The true disparity of reduction degree between calcined and plasma treated catalysts should be smaller than the listed data.

3.2. Catalytic behavior in steam reforming of glycerol reaction

Glycerol steam reforming reactions using the four Ni/CeO₂ catalysts were carried out under ambient pressure and at 450 °C, reaction data at 8 h of reaction are listed in Table 5. Fig. 6 shows the glycerol conversion as a function of time on steam, all the four catalysts showed a 100% initial conversion of glycerol. It is reported that the active sites for steam reforming of glycerol are located on metallic Ni⁰, and their numbers are in direct proportional to both the nickel dispersion and its reducibility [4,11,46,47]. In this work, the four catalysts had relatively high nickel dispersion and reducibility, even for the two calcined samples. Thus, a 100% of glycerol conversion was observed on all the catalysts. With increasing time on stream, rapid deactivation was clearly occurred firstly on Ni-N/CeO₂-C, and then Ni-Cl/CeO₂-C catalyst was also started to deactivate after 6 h of reaction; whereas no

Table 5
Glycerol steam reforming performance of the four Ni/CeO₂ catalysts.

Catalyst	Glycerol conversion (%)	Products selectivity (%)			
		H ₂	CO ₂	CO	CH ₄
Ni-N/CeO ₂ -C	83.0	14.0	14.6	84.8	0.6
Ni-N/CeO ₂ -P	100	44.7	44.8	54.6	0.6
Ni-Cl/CeO ₂ -C	96.9	34.2	29.3	70.4	0.3
Ni-Cl/CeO ₂ -P	100	38.7	39.1	59.9	1.0

deactivation was observed on the two plasma treated catalysts Ni-N/CeO₂-P and Ni-Cl/CeO₂-P throughout the 8 h of reaction. Plasma treated catalysts showed better reaction stability than the calcined counterparts.

Table 5 shows products selectivities varied with both precursor decomposition manner and nickel sources. Higher H₂ selectivity was observed on the catalysts using nickel chloride as precursor and particularly on the ones with glow discharge plasma treatment. The two plasma treated catalysts which displayed the best reaction stability also had the highest H₂ selectivity, as well as the lowest selectivity of CO. The higher H₂ selectivity was due to the higher water gas shift reaction activity on plasma treated and nickel chloride prepared catalysts. Besides, it's good to see that methanation reaction of CO as a side reaction was quite faint in this catalytic system.

3.3. Structure and properties of spent catalysts

XRD, TEM, Raman and thermal analysis of spent catalysts were performed to explore the reasons for reaction deactivation, and to better understand the good reaction stability on plasma treated catalysts. XRD patterns of spent catalysts are shown in Fig. 7, which illustrated that still no peak assigned to nickel species was observed on Ni-N/CeO₂-P sample, indicating the maintaining of high nickel dispersion on this catalyst during reduction and reaction process. As to the other three catalysts (both calcined catalysts and Ni-Cl/CeO₂-P), diffraction peaks of Ni⁰ with different intensities were observed, the metallic Ni particle sizes calculated by Scherrer equation based on the diffraction of Ni⁰ (111) crystal plane at 44.4° are listed in Table 6. Sintering of Ni species was occurred on all three above mentioned catalysts, particularly for Ni-Cl/CeO₂-C catalyst, the augment of average Ni particle size was quite significant.

To better illustrate the dispersion change of nickel species, TEM images and nickel particle size distributions of the spent catalysts are shown in Fig. 8, the data are also listed in Table 6. Compare with those of the fresh prepared catalysts (Fig. 3), and combined the particle size data obtained from XRD (Table 6), no severe sintering of nickel species was observed on all four catalysts, and the particle size growth on the catalysts prepared from nickel chloride was slightly more significant than the ones using nickel nitrate as source. It was found that Ni-Cl/CeO₂ (-C or -P) catalysts had stronger Ni-Ce interaction than Ni-N/CeO₂ counterparts, however, stronger sintering was observed on former catalysts, this phenomena may due to the presence of Cl⁻, which is hard to be removed via calcination or reduction and could accelerate the occurrence of sintering [16]. Nickel particle growth by Ostwald ripening is considered as one of the major reasons for catalytic deactivation [48], however, since only slightly nickel particle growth was found on the fastest deactivated Ni-N/CeO₂-C catalyst, nickel sintering may contribute to but not the main reason for the deactivation of GSR reaction in this work.

Coke deposition is also one of the most important factors for reaction deactivation, through the TEM images of the four spent catalysts, carbonaceous deposition was only observed on the two calcined samples, and the representative images are shown in Fig. S6. Although apparent carbon deposition was both occurred on two calcined catalysts, the deposited carbon species on these two samples were seemed in different shapes. On spent Ni-N/CeO₂-C catalyst, typically graphitic

Table 6
Nickel particle size of oxidized, reduced and spent catalysts obtained from XRD and TEM.

Catalyst	d_{NiO} (nm, XRD, oxidized)	d_{NiO} (nm, TEM, oxidized)	d_{Ni} (nm, XRD, reduced)	d_{Ni} (nm, XRD, spent)	d_{Ni} (nm, TEM, spent)
Ni-N/CeO ₂ -C	16.4	10.4	14.5	17.3	12.2
Ni-N/CeO ₂ -P	Not detected	6.0	–	Not detected	7.9
Ni-Cl/CeO ₂ -C	29.8	12.6	26.8	46.3	18.9
Ni-Cl/CeO ₂ -P	Not detected	7.5	10.5	11.3	9.8

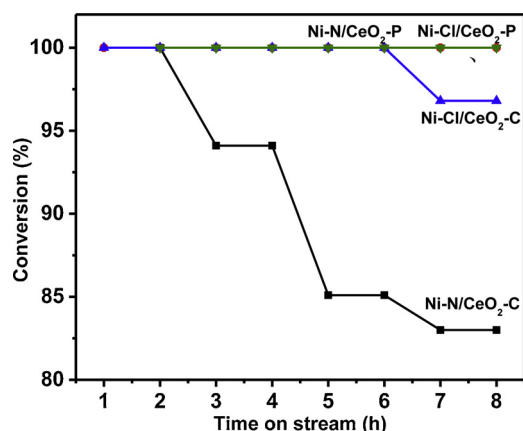


Fig. 6. Glycerol conversion as a function of reaction time on stream.

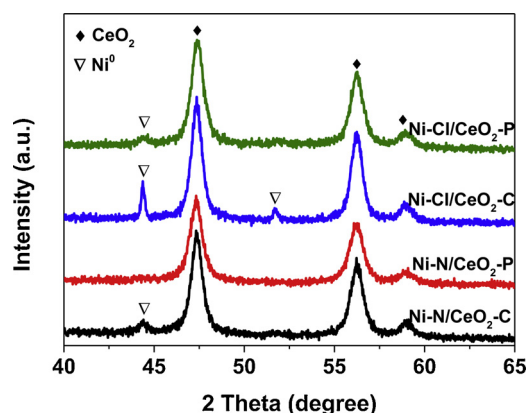


Fig. 7. XRD patterns of spent catalysts.

fibrous carbon was apparently represented. While on spent Ni-Cl/CeO₂-C catalyst, the carbon species were more in amorphous form and seemed to clump together.

Raman spectroscopy in the range of 50–2000 cm^{−1} was performed to get information about the nature of deposited carbon species in spent catalysts. The F_{2g} peak of CeO₂ at ~452 cm^{−1} [49,50] was measured and calibrated to the same intensity, for better comparison the intensity of carbon species, as shown in Fig. 9(a). The carbonaceous modes in two plasma treated catalysts showed very weak peak intensities, while much stronger carbon Raman peaks were observed on calcined samples, particularly on the one prepared with nickel nitrate (Ni-N/CeO₂-C). These observations are consistent with TEM results up ahead. Besides the generally well known D band (~1355 cm^{−1}, disordered peak) and G band (~1575 cm^{−1}, ordered peak), a peak located around 1200 cm^{−1} was also clearly presented in all four spent samples. According to refs. [15,51,52], after carefully peak-differentiating (Fig. 9(b)), the Raman peaks in the range of 1000–1700 cm^{−1} can be divided into four peaks and identified as sp³-rich phase of the amorphous carbon at ~1200 cm^{−1}, D peak microcrystalline highly disordered sp² graphitic structure at ~1340 cm^{−1}, vibrations of C–H in hydrogenated amorphous carbon at ~1500 cm^{−1}, and G peak of highly ordered sp² graphite at ~1590 cm^{−1}.

Based on the above identification, differences of deposited carbon species were revealed, compared with the two calcined catalysts, nickel chloride instead of nickel nitrate as nickel source would lead to a slightly increase of sp³-rich phase of the amorphous carbon (7.5%–8.3%) and decreases of ordered sp² graphitic structure (29.2%–27.2%). As to the plasma treated samples, this tendency was also revealed, and in spent Ni-Cl/CeO₂-P catalyst, only faint peak assigned to 100% sp³-rich phase of the amorphous carbon was observed.

Fig. 10 shows the thermogravimetric analysis (TGA) curves of the four spent Ni/CeO₂ catalysts in air atmosphere. The weight loss below 200 °C was considered as the vaporization of adsorbed water, and that in the range of 200–700 °C can be ascribed to the combustion of carbonaceous species. A slight weight increase was observed on some of the samples between 200–400 °C, which could be attributed to the re-oxidation of the metallic Ni⁰ species in spent catalysts. DTG profiles of the spent catalysts show peaks in three regions, the first peak located below 200 °C was originated by the loss of water, and two other peaks in the range of 250–400 °C and 450–650 °C were due to the gasification of carbon species. The appearance of these two peaks and their allocation proportion suggested the presence of two types of carbonaceous species. Combined with TEM and Raman findings, the high temperature exothermic peaks at 530–560 °C were from the combustion of sp² graphitic carbon, while the peaks at 320–340 °C were corresponded to the gasification of amorphous carbon species [11]. The quantified results listed in Table 7 shows that the coke amount and formation rate were in the order of Ni-N/CeO₂-C > Ni-Cl/CeO₂-C > Ni-N/CeO₂-P ≈ Ni-Cl/CeO₂-P. Much higher coke deposition rate was found on Ni-N/CeO₂-C catalyst.

Sintering of Ni⁰ and coke deposition are known as the two major reasons responsible for catalytic deactivation. In this work, deactivation was observed only on the two calcined catalysts. Since much severe sintering were occurred on Ni-Cl/CeO₂-C catalyst than that on Ni-N/CeO₂-C, but the deactivation rate on former catalyst was much smaller than that on latter one, therefore, the deactivation behavior of the catalysts in this work was more closely related to the deposited carbonaceous species. Apparent coke deposition on the two calcined catalysts was the most likely reason for their deactivation in glycerol steaming reforming reaction. Besides the coke formation amount, type of carbonaceous species may be also an influence parameter. Based on the characterization results of spent catalysts, the samples prepared from nickel nitrate tended to form fibrous graphite carbon species, while those from nickel chloride formed amorphous carbon as well.

It is documented that the formation of solid carbon species on catalyst surface was either by CO disproportionation or CH₄ decomposition [53–55], since CH₄ selectivity in this catalytic system was quite low (< 1%), coke deposition were mostly originated from CO disproportionation. CO dissociation on Ni active sites could firstly generate highly reactive carbon species (C_a), which would be mostly gasified in the presence of CO₂, H₂ and H₂O, and partially converted into less active carbon species (C_p). The less active carbon species (C_p) would be either gasified or encapsulated on the catalyst surface or dissolved in the nickel particles [55,56]. Above results showed that plasma treatment could greatly diminish the carbon deposition rate by enhancing the gasification ability of dissociated carbon species, while nickel source may influence the carbon deposition manners. The atomic carbon species on the catalysts prepared by nickel nitrate was preferred

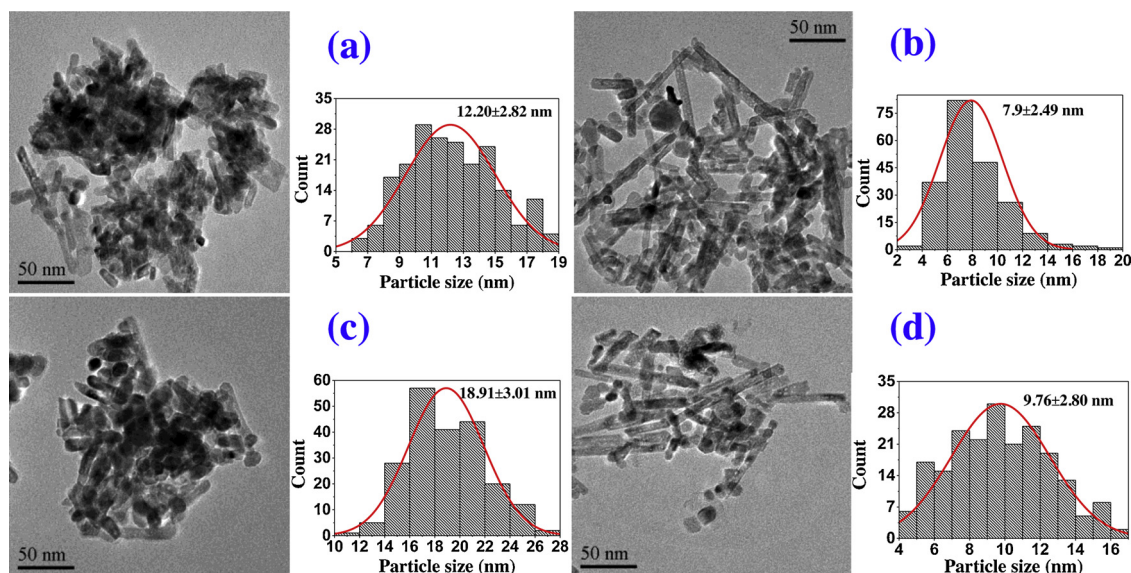


Fig. 8. TEM images and particle size distributions of nickel species of spent catalysts, (a) Ni-N/CeO₂-C; (b) Ni-N/CeO₂-P; (c) Ni-Cl/CeO₂-C; (d) Ni-Cl/CeO₂-P.

to diffuse through nickel to nucleate and form graphite like carbon species; whereas that on the ones prepared by nickel chloride was more likely to encapsulate in the form of amorphous carbon.

Combined with the catalytic data, coke deposition were more effective in diminishing the number of active Ni²⁺ sites and resulting in continuous deactivation than sintering. As to the two plasma treated catalysts, glow discharge plasma could effectively decomposed the nickel salts, and benefit for the fast nucleation and slow crystallite growth, the obtained nickel particles were much smaller and homogeneously dispersed [22]. Besides, the small NiO particles generated in plasma field were tend to incorporated with CeO₂ support to form Ni-O-Ce composite, and the generated adsorbed oxygen species not only guaranteed the high Ni reducibility, but also hindered the coke formation on plasma treated catalysts. Much higher nickel dispersion as well as much lower coke deposition rate maintained the reaction at high activity.

4. Conclusions

The impacts of nickel sources and dried precursors decomposition methods on catalytic performance in glycerol steam reforming reaction over Ni/CeO₂ catalysts were investigated. Glow discharge plasma treatment could remarkably enhance the nickel dispersion and Ni-Ce interaction; meanwhile, lead to the formation of Ni-O-Ce composite. As

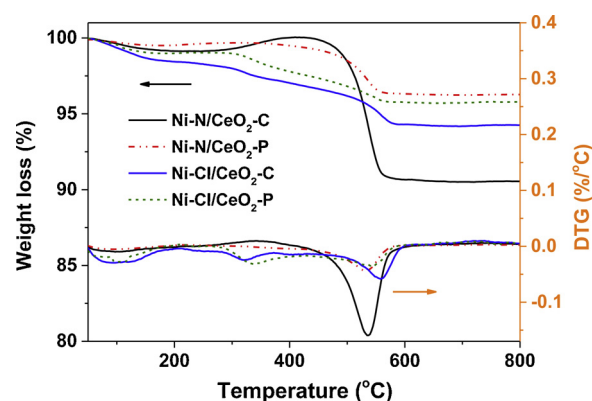


Fig. 10. TGA and DTG curves of the spent Ni/CeO₂ catalysts.

a result, the plasma treated catalysts showed enhanced H₂ selectivity and reaction stability, in comparison with the calcined counterparts.

Compared with the catalysts prepared with nickel nitrate, nickel chloride prepared catalysts had comparatively larger nickel particles, meanwhile, stronger Ni-CeO₂ interaction and slower carbon deposition rate. In addition, the carbonaceous species formed on the Ni-Cl/CeO₂ catalysts during reaction were more in the form of amorphous carbon. Carbonaceous deposition contributed more to deactivation of GSR

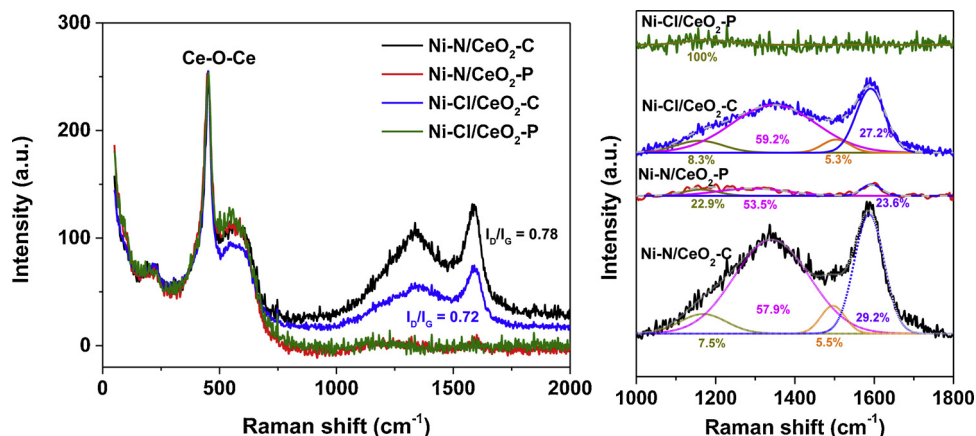


Fig. 9. Raman spectra of four spent catalysts.

Table 7

Quantitative data of coke deposition for the spent catalysts based on TG analysis.

Catalyst	Temperature range (°C)	Weight loss (%)	Coke (mg _C /(g _{cat} ·h))
Ni-N/CeO ₂ -C	414–700	9.52	11.90
Ni-N/CeO ₂ -P	312–700	3.36	4.20
Ni-Cl/CeO ₂ -C	200–700	4.27	5.34
Ni-Cl/CeO ₂ -P	255–700	3.30	4.13

reaction than nickel particle sintering, therefore, Ni-Cl/CeO₂ catalysts presented good reaction stability, particularly for the comparison of calcined Ni-N/CeO₂-C catalyst.

Acknowledgements

We thank the financial support by National Natural Science foundation of China (21203255, 21473259, 21603153), Hubei Natural Science Foundation (2018CFB556), Science and Technology Department of Sichuan Province (No. 2016HH0026), Technology Foundation for Selected Overseas Chinese Scholar, Ministry of Personnel of China (BZY14037), the Fundamental Research Funds for the Central Universities (South-Central University for Nationalities, CZY19006) and the Fund for Basic Scientific Research of South-Central University for Nationalities (YZZ12001).

Appendix A. Supplementary data

Supplementary material related to this article can be found, in the online version, at doi:<https://doi.org/10.1016/j.apcatb.2019.02.074>.

References

- [1] S. Liu, Z. Yan, Y. Zhang, R. Wang, S.-Z. Luo, F. Jing, W. Chu, *ACS Sustain. Chem. Eng.* 6 (11) (2018) 14403–14413, <https://doi.org/10.1021/acssuschemeng.1028b03095>.
- [2] Q. Zhuang, P. Geddis, A. Runstedtler, B. Clements, *Fuel* 209 (2017) 76–84.
- [3] Z. Wei, J. Sun, Y. Li, A.K. Datye, Y. Wang, *Chem. Soc. Rev.* 41 (2012) 7994–8008.
- [4] A.J. Reynoso, J.L. Ayastuy, U. Iriarte-Velasco, M.A. Gutiérrez-Ortiz, *Appl. Catal. B: Environ.* 239 (2018) 86–101.
- [5] K.K. Mandari, J.Y. Do, A.K.R. Police, M. Kang, *Appl. Catal. B: Environ.* 231 (2018) 137–150.
- [6] W. Fang, S. Paul, M. Capron, A.V. Biradar, S.B. Umbarkar, M.K. Dongare, F. Dumeignil, L. Jalowiecki-Duhamel, *Appl. Catal. B: Environ.* 166–167 (2015) 485–496.
- [7] W. Fang, C. Pirez, S. Paul, M. Capron, H. Jobic, F. Dumeignil, L. Jalowiecki-Duhamel, *ChemCatChem* 5 (2013) 2207–2216.
- [8] N.H. Tran, G.S.K. Kannangara, *Chem. Soc. Rev.* 42 (2013) 9454–9479.
- [9] X. Huang, C. Dang, H. Yu, H. Wang, F. Peng, *ACS Catal.* 5 (2015) 1155–1163.
- [10] G. Wu, C. Zhang, S. Li, Z. Han, T. Wang, X. Ma, J. Gong, *ACS Sustain. Chem. Eng.* 1 (2013) 1052–1062.
- [11] Z. Yan, S. Liu, Y. Zhang, T. Wang, S. Luo, W. Chu, F. Jing, *Catal. Today* 319 (2018) 229–238.
- [12] C. Pirez, W. Fang, M. Capron, S. Paul, H. Jobic, F. Dumeignil, L. Jalowiecki-Duhamel, *Appl. Catal. A: Gen.* 518 (2016) 78–86.
- [13] W. Fang, C. Pirez, S. Paul, M. Jiménez-Ruiz, H. Jobic, F. Dumeignil, L. Jalowiecki-Duhamel, *Int. J. Hydrogen Energy* 41 (2016) 15443–15452.
- [14] W. Fang, Y. Romani, Y. Wei, M. Jiménez-Ruiz, H. Jobic, S. Paul, L. Jalowiecki-Duhamel, *Int. J. Hydrogen Energy* 43 (2018) 17643–17655.
- [15] G. Słowik, M. Greluk, M. Rotko, A. Machocki, *Appl. Catal. B: Environ.* 221 (2018) 490–509.
- [16] Z. Yu, X. Hu, P. Jia, Z. Zhang, D. Dong, G. Hu, S. Hu, Y. Wang, J. Xiang, *Appl. Catal. B: Environ.* 237 (2018) 538–553.
- [17] S. Liu, J. Mei, C. Zhang, J. Zhang, R. Shi, J. Mater. Sci. Technol. 34 (2018) 836–841.
- [18] A.D. Shejale, G.D. Yadav, *Ind. Eng. Chem. Res.* 57 (2018) 4785–4797.
- [19] M. Zhang, S. Wu, L. Bian, Q. Cao, W. Fang, *Catal. Sci. Technol.* 9 (2019) 286–301.
- [20] C.-j. Liu, G.P. Vissokov, B.W.L. Jang, *Catal. Today* 72 (2002) 173–184.
- [21] C. Liu, M. Li, J. Wang, X. Zhou, Q. Guo, J. Yan, Y. Li, *Chin. J. Catal.* 37 (2016) 340–348.
- [22] Z. Wang, Y. Zhang, E.C. Neyts, X. Cao, X. Zhang, B.W.L. Jang, C.-j. Liu, *ACS Catal.* 8 (2018) 2093–2110.
- [23] L. Zhao, Y. Wang, Z. Sun, A. Wang, X. Li, C. Song, Y. Hu, *Green Chem.* 16 (2014) 2619–2626.
- [24] S. Zhang, C.-Y. Chen, B.W.L. Jang, A.-M. Zhu, *Catal. Today* 256 (2015) 161–169.
- [25] D. Chen, M. Qiao, Y.-R. Lu, L. Hao, D. Liu, C.-L. Dong, Y. Li, S. Wang, *Angew. Chem. Int. Ed.* 57 (2018) 8691–8696.
- [26] C. Liu, J. Lan, F. Sun, Y. Zhang, J. Li, J. Hong, *RSC Adv.* 6 (2016) 57701–57708.
- [27] J. Hong, J. Du, B. Wang, Y. Zhang, C. Liu, H. Xiong, F. Sun, S. Chen, J. Li, *ACS Catal.* 8 (2018) 6177–6185.
- [28] J.G. Seo, M.H. Youn, S. Park, J.S. Chung, I.K. Song, *Int. J. Hydrogen Energy* 34 (2009) 3755–3763.
- [29] G. Jacobs, T.K. Das, Y. Zhang, J. Li, G. Racoillet, B.H. Davis, *Appl. Catal. A: Gen.* 233 (2002) 263–281.
- [30] M.-S. Fan, A.Z. Abdullah, S. Bhatia, *Appl. Catal. B: Environ.* 100 (2010) 365–377.
- [31] S.H. Gage, D.A. Ruddy, S. Pylypenko, R.M. Richards, *Catal. Today* 306 (2018) 9–15.
- [32] E. Soghrati, T.K.C. Ong, C.K. Poh, S. Kawi, A. Borgna, *Appl. Catal. B: Environ.* 235 (2018) 130–142.
- [33] W. She, T. Qi, M. Cui, P. Yan, S.W. Ng, W. Li, G. Li, *ACS Appl. Mat. Interfaces* 10 (2018) 14698–14707.
- [34] M.S.P. Francisco, V.R. Mastelaro, P.A.P. Nascente, A.O. Florentino, *J. Phys. Chem. B* 105 (2001) 10515–10522.
- [35] L. Liu, Z. Yao, Y. Deng, F. Gao, B. Liu, L. Dong, *ChemCatChem* 3 (2011) 978–989.
- [36] L. Vivier, D. Duprez, *ChemSusChem* 3 (2010) 654–678.
- [37] S. Zhang, C.-R. Chang, Z.-Q. Huang, J. Li, Z. Wu, Y. Ma, Z. Zhang, Y. Wang, Y. Qu, *J. Am. Chem. Soc.* 138 (2016) 2629–2637.
- [38] Y. Li, B. Zhang, X. Tang, Y. Xu, W. Shen, *Catal. Comm.* 7 (2006) 380–386.
- [39] W. Shan, M. Luo, P. Ying, W. Shen, C. Li, *Appl. Catal. A: Gen.* 246 (2003) 1–9.
- [40] G. Jacobs, P.M. Patterson, Y. Zhang, T. Das, J. Li, B.H. Davis, *Appl. Catal. A: Gen.* 233 (2002) 215–226.
- [41] A.Y. Khodakov, A. Griboval-Constant, R. Bechara, V.L. Zholobenko, *J. Catal.* 206 (2002) 230–241.
- [42] P. Ganesan, H.K. Kuo, A. Saavedra, R.J. De Angelis, *J. Catal.* 52 (1978) 310–320.
- [43] S. Dou, L. Tao, J. Huo, S. Wang, L. Dai, *Energy Environ. Sci.* 9 (2016) 1320–1326.
- [44] T.K. Das, G. Jacobs, P.M. Patterson, W.A. Conner, J. Li, B.H. Davis, *Fuel* 82 (2003) 805–815.
- [45] C. Liu, H. Liu, B. Wang, J. Hong, F. Zhao, F. Sun, C. Liu, Y. Zhang, J. Li, *Energy Technol.* 7 (2) (2019) 224–232, <https://doi.org/10.1002/ente.201800669>.
- [46] N. Sánchez, J.M. Encinar, J.F. González, *Ind. Eng. Chem. Res.* 55 (2016) 3736–3741.
- [47] N.H. Zamzuri, R. Mat, N.A. Saidina Amin, A. Talebian-Kiakalaieh, *Int. J. Hydrogen Energy* 42 (2017) 9087–9098.
- [48] P. Munnik, M.E.Z. Velthoen, P.E. de Jongh, K.P. de Jong, C.J. Gommers, *Angew. Chem. Int. Ed.* 126 (2014) 9647–9651.
- [49] E. Swatsitang, S. Phokha, S. Hunpratub, S. Maensiri, *Mater. Des.* 108 (2016) 27–33.
- [50] S. Phokha, S. Hunpratub, B. Usher, A. Pimsawat, N. Chanlek, S. Maensiri, *Appl. Surf. Sci.* 446 (2018) 36–46.
- [51] Y. Wang, D.C. Alsmeyer, R.L. McCreery, *Chem. Mater.* 2 (1990) 557–563.
- [52] J. Schwan, S. Ulrich, V. Batori, H. Ehrhardt, S.R.P. Silva, *J. Appl. Phys.* 80 (1996) 440–447.
- [53] J. Rostrup-Nielsen, D.L. Trimm, *J. Catal.* 48 (1977) 155–165.
- [54] D.L. Trimm, *Catal. Today* 49 (1999) 3–10.
- [55] X. Yan, B. Zhao, Y. Liu, Y. Li, *Catal. Today* 256 (2015) 29–40.
- [56] D.L. Trimm, *Catal. Today* 37 (1997) 233–238.